High pressure effect in nanoporous carbon materials: Effects of pore geometry

Yun Long [a], Małgorzata Śliwińska-Bartkowiak [b], Henryk Drozdowski [b], Mateusz Kempiński [b], Katherine A. Phillips [a], Jeremy C. Palmer [a], Keith E. Gubbins [a,*]

[a] Department of Chemical and Biomolecular Engineering, North Carolina State University, Raleigh, NC 27695-7905, USA
[b] Institute of Physics, Adam Mickiewicz University, Umultowska 85,61-614 Poznan, Poland

HIGHLIGHTS

► Pressure in carbon pores of various shapes by molecular simulation and experiments.
► The normal pressure oscillates with pore size and expands or compresses the pore.
► The pressure of adsorbate in the pore is enhanced by a factor of 10^3–10^5.
► The curvature of pore wall surface enhances the in-pore pressure additionally.
► The tangential pressure increases rapidly with the bulk pressure.

GRAPHICAL ABSTRACT
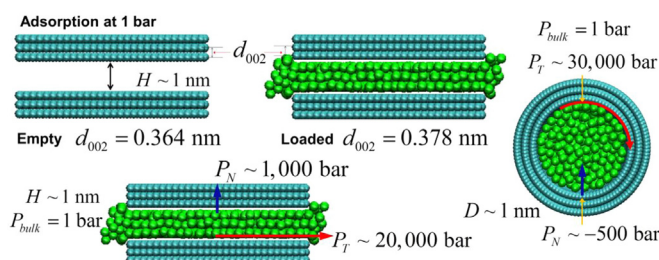
ARTICLE INFO

ABSTRACT

Abundant experimental evidence suggests that adsorbates confined in nanoporous materials exhibit high pressures, such as high pressure crystal structures, high pressure chemical reactions, and the deformation of pore walls due to the adsorbate. We report molecular simulation studies of the pressure tensor for simple adsorbates (e.g. argon) in carbon nanopores of slit, cylindrical and spherical geometries. We find that for modest bulk phase pressures of 1 bar or less, the pressures parallel to the pore walls (tangential pressure) is of the order 10^4–10^5 bar, while the pressure normal to the wall is of the order of 10^3 bar, and can be positive or negative depending on the pore size. Moreover, we find that the pore geometry has a large effect on the structure of the adsorbate and thus on the in-pore pressure because of the curvature that determines the strength of the adsorbate–wall interaction. For the same pore size, temperature and bulk pressure, the in-pore tangential pressure is the largest in spherical pores, followed by that in cylindrical pores and slit pores. We also study the normal pressure of carbon tetrachloride and water confined in activated carbon fibers by molecular simulations and experiments. The pressure acting on the pore wall is found to be of the order of several thousand bar by both methods. Experiments also find that the pore can be expanded or contracted, depending on pore width, as we predict by molecular simulation.

© 2012 Elsevier B.V. All rights reserved.

1. Introduction

Numerous experimental studies have observed phenomena for a confined phase within a nanopore that only occur at very high pressures (e.g. $\sim 10^4$ bar) for the bulk phase, even though the pressure of the bulk phase in equilibrium with the nanoporous material is 1 bar or less. Examples include the occurrence of high pressure chemical reactions (e.g., high yield of dimerization of nitric oxide in nanopores [1,2]), formation of high pressure crystal phases (e.g., formation of ice VIII and IV in nanotubes [3] and KI B2 structure in carbon nanohorns [4]), high pressure effects in solid–liquid equilibrium (e.g., the increase in freezing points of cyclohexane and

n-dodecane in activated carbon fibers and nanotubes [5–8]), and effects on spectral properties, all of which occur for the phases confined in the nanopores and in equilibrium with the bulk phase at atmospheric pressure. Moreover, experimental small-angle X-ray scattering studies show significant effects of the adsorption of a confined phase on the pore width and interlayer atomic spacing of the pore walls, indicating a strong positive or negative pressure normal to the walls. [9,10]

Molecular simulation studies of the pressure tensor components have been reported for simple fluids confined in the nanopores of slit shape. [11,12] In this study, we perform fluid adsorption in carbon pore models with various geometries. We calculate the pressure tensor components (the pressure normal to the wall and the pressure parallel to the wall surface) for these pore models, which allows us to study the effects of the pore geometry. We also report experimental results for a nonpolar (CCl_4) and polar (H_2O) fluid in activated carbon fibers, showing the material deformation due to the adsorption and the pressure, and estimate the experimental in-pore pressure normal to the wall by using the Young's relationship between the stress (pressure) and strain (material deformation).

2. Models and methods

2.1. Theory and simulation details

Pressure is the force per unit area acting on a surface element and is the sum of a kinetic contribution which arises from the convective momentum transport of molecules and a configurational contribution which arises from interactions among molecules. For inhomogeneous fluids pressure is a second-order tensor, **P**, whose component $P_{\alpha\beta}$ gives the force per unit area in the β-direction on a surface pointing in the α-direction. Because of the geometrical symmetry and system orthogonality, the off-diagonal components of the pressure tensor of the adsorbate confined in planar, cylindrical and spherical pores are zero, while the non-trivial diagonal components are only functions of the distance between a position in space and the wall surface. For example, in the slit pore, the tangential pressure (parallel to the walls, which lie in the xy-plane) $P_{xx} = P_{yy} = P_T$ and the normal pressure (pointing to the wall) $P_{zz} = P_N$ only depend on z. Similarly, in the cylindrical pore, using cylindrical polar coordinates (ρ, φ, z), the tangential pressure in the ϕ-direction $P_{\phi\phi} = P_{T\phi}$, the tangential pressure in the z-direction $P_{zz} = P_{Tz}$, and the normal pressure $P_{\rho\rho} = P_N$ are only functions of the radial coordinate ρ. In spherical pores, the tangential pressure in the ϕ- and θ-directions $P_{\phi\phi} = P_{\theta\theta} = P_T$ and the normal pressure $P_{\rho\rho} = P_N$ are only functions of the radial coordinate ρ. [13] These can be expressed mathematically in Eq. (1):

$$\mathbf{P} = \mathbf{P}_{kin} + \mathbf{P}_{conf} = \left\{ \begin{array}{l} \begin{bmatrix} P_T(z) & 0 & 0 \\ 0 & P_T(z) & 0 \\ 0 & 0 & P_N(z) \end{bmatrix} \text{(slit)} \\ \begin{bmatrix} P_N(\rho) & 0 & 0 \\ 0 & P_{T\varphi}(\rho) & 0 \\ 0 & 0 & P_{Tz}(\rho) \end{bmatrix} \text{(cylinder)} \\ \begin{bmatrix} P_N(\rho) & 0 & 0 \\ 0 & P_T(\rho) & 0 \\ 0 & 0 & P_T(\rho) \end{bmatrix} \text{(sphere)} \end{array} \right. \quad (1)$$

Equilibrium between the confined and bulk phases requires, in addition to the usual thermodynamic conditions (equality of temperatures and chemical potentials), hydrostatic equilibrium (i.e. no net momentum transfer between the two phases). In the absence

of external fields this latter condition can be expressed as $\nabla \cdot \mathbf{P} = 0$ [13,14]. In the simulations, for this condition to be satisfied in general the confined phase must be in physical contact with the bulk phase. However, if the wall atoms are fixed in space the condition is satisfied in grand canonical Monte Carlo simulations without the necessity of such physical contact [14]. The hydrostatic stability condition leads to useful results and relations for the pressure components:

$$\text{Slit}: P_N = \text{constant (independent of } z)$$

$$\text{Cylinder}: P_{T\varphi}(\rho) = P_N(\rho) + \rho \frac{dP_N(\rho)}{d\rho} \quad (2)$$

$$\text{Sphere}: P_T(\rho) = P_N(\rho) + \frac{\rho}{2} \frac{dP_N(\rho)}{d\rho}$$

The pressure tensor can be calculated by either the virial route or thermodynamic route. For fluids composed of spherical molecules, where only pairwise additive potentials exist, the pressure tensor can be expressed as

$$\mathbf{P}(\mathbf{r}) = \rho_{ad}(\mathbf{r})k_BT\mathbf{1} - \frac{1}{2}\left\langle \sum_{i \neq j} \frac{\partial u(ij)}{\partial \mathbf{r}_{ij}} \int_{C_{ij}} \widetilde{dl}\delta(\mathbf{r} - \widetilde{l}) \right\rangle, \quad (3)$$

where $\mathbf{r}$ is the position vector, $\rho_{ad}(\mathbf{r})$ is the local number density of the molecules, k_B is Boltzmann constant, T is the temperature and $\mathbf{1}$ is the unit tensor, i and j are indices of molecules, $u(ij)$ is the pairwise potential between molecules i and j, C_{ij} is any arbitrary contour connecting the centre of mass of molecule i, $\mathbf{r}_i$, to the centre of mass of molecule j, $\mathbf{r}_j$, $\mathbf{r}_{ij} = \mathbf{r}_j - \mathbf{r}_i$ and $\delta(x)$ is the Dirac delta function. The first term of the righ-hand side in Eq. (3) is the well-defined kinetic contribution. The second term is the configurational contribution, and for an inhomogeneous system, different choices of the contour C_{ij} will lead to different definitions of the pressure tensor.

Here we adopt the widely used Irving–Kirkwood definition of **P**, in which C_{ij} is chosen to be a straight line connecting the centres of molecules i and j: $C_{ij} = \{\widetilde{l}|\widetilde{l} = \lambda \mathbf{r}_{ij} + \mathbf{r}_i; \quad 0 \leq \lambda \leq 1\}$. For the planar surface (slit pore case), the mathematical expression of the Irving–Kirkwood definition can be written as [15]

$$P_{\alpha\alpha}^{IK}(z_k) = \rho_{ad}(z_k)k_BT\mathbf{1}$$
$$- \frac{1}{2A}\left\langle \sum_{i \neq j} \frac{(\mathbf{r}_{ij})_\alpha(\mathbf{r}_{ij})_\alpha}{r_{ij}} \frac{u'(r_{ij})}{|z_{ij}|} \theta\left(\frac{z_k - z_i}{z_{ij}}\right) \theta\left(\frac{z_j - z_k}{z_{ij}}\right) \right\rangle, \quad (4)$$

where z_k is the z-coordinate for the plane where the pressure tensor is evaluated, α represents x-, y- or z-directions, $\theta(x)$ is the Heaviside step function, $u'(r) = du(r)/dr$ and A is the surface area of the z-plane. Two Heaviside step functions in Eq. (4) mathematically indicate that the interaction between molecules i and j contributes to the pressure tensor at plane $z = z_k$ if the straight line between molecules i and j passes through that plane. The tangential and normal components of the pressure tensor for a planar surface can be written as

$$P_T^{IK}(z_k) = \rho_{ad}(z_k)k_BT$$
$$- \frac{1}{4A}\left\langle \sum_{i \neq j} \frac{x_{ij}^2 + y_{ij}^2}{r_{ij}} \frac{u'(r_{ij})}{|z_{ij}|} \theta\left(\frac{z_k - z_i}{z_{ij}}\right) \theta\left(\frac{z_j - z_k}{z_{ij}}\right) \right\rangle, \quad (5)$$

$$P_N^{IK}(z_k) = \rho_{ad}(z_k)k_BT$$
$$- \frac{1}{2A}\left\langle \sum_{i \neq j} \frac{z_{ij}^2}{r_{ij}} \frac{u'(r_{ij})}{|z_{ij}|} \theta\left(\frac{z_k - z_i}{z_{ij}}\right) \theta\left(\frac{z_j - z_k}{z_{ij}}\right) \right\rangle. \quad (6)$$

Eqs. (5) and (6) are convenient for computer coding. For the spherical surface, the mathematical expression of Irving–Kirkwood definition can be written as:

$$P_N^{IK}(\rho) = \rho_{ad}(\rho)k_BT - \frac{1}{8\pi\rho^2}$$

$$\left\langle \sum_{i\neq j}\sum_{k=1}^{2} |\mathbf{r}_{ij}\mathbf{e}_l(\alpha_{k(ij)})| \frac{u'(r_{ij})}{r_{ij}} \theta(\alpha_{k(ij)})\theta(1-\alpha_{k(ij)}) \right\rangle \quad (7)$$

$$P_T^{IK}(\rho) = \rho_{ad}(\rho)k_BT$$

$$-\frac{1}{4\pi\rho\Delta}\left\langle \sum_{i\neq j} |\mathbf{r}_{ij}\mathbf{e}_\varphi| \frac{u'(r_{ij})}{r_{ij}} \theta(\rho+\Delta-l(\lambda_{ij}))\theta(l(\lambda_{ij})-\rho+\Delta)\theta(\lambda_{ij})\theta \right.$$

$$\left. (1-\lambda_{ij}) \right\rangle . \tag{8}$$

where $\mathbf{e}_l$ and $\mathbf{e}_\phi$ are unit vectors in the ρ- and ϕ-directions at the evaluated positions (not constants as in the Cartesian system), respectively; $\delta(x)$ is the Dirac Delta function; Δ is a tiny radial increment by which the sphere is divided into bins in the radial direction; $\alpha_{k(ij)}$ and λ_{ij} are roots of the equations generated during the derivation. The detailed derivation and definitions of symbols can be found in the appendix which is based on [16]. The results for the in-pore pressure in this paper are calculated using the virial (or mechanical) route and Irving–Kirkwood definition, unless otherwise indicated (some are from the volume perturbation method, mentioned below). The normal pressure of the adsorbate acting on the wall, which can cause deformation of the wall material, can be evaluated by summing up the normal components of the intermolecular forces between all the pairs of adsorbate molecules and wall atoms and dividing by the area of the wall inner surface.

Besides the virial route, pressure tensor can also be calculated from the thermodynamic route: in the canonical ensemble the pressure is given by $P = -(\partial A/\partial V)_{N,T}$, where A is the Helmholtz energy, so that it can be obtained by calculating the small changes in A for a series of small perturbations in V. This is also called the volume perturbation method. For a slit pore system, the normal pressure of the adsorbate, which should be a constant through the pore (except near the pore mouth), can be obtained by evaluating the change in Helmholtz free energy when the volume change arises only from a change in the z-dimension, keeping the dimensions in x and y directions constant [17]:

$$P_N^V = -\left(\frac{\partial A}{\partial V}\right)_{N,T,L_x,L_z} = \rho_{ad}k_BT$$

$$- Lim_{\Delta L_z \to 0} \frac{k_BT}{L_xL_y\Delta L_z} \ln < e^{-\Delta U/k_BT} >_0, \tag{9}$$

where ΔU is the configurational energy difference between the perturbed and unperturbed systems, and $<...>_0$ indicates an ensemble average over the unperturbed system of volume V. The perturbation is carried out by scaling the z-coordinates of all the adsorbate molecules and wall atoms by a factor $(1+\xi)$, so that $\Delta L_z = \xi L_z$. In this paper, only the normal pressure of water confined in the carbon slit pore is calculated by this method.

To study the effects of pore geometry on the adsorption and pressure of the confined adsorbate, slit, cylindrical and spherical carbon pores were constructed, as shown in Fig. 1. For the slit pore (Fig. 1a), the pore walls consist of three graphene layers lying in the xy-plane of dimension $L_x = 6.8$ nm, $L_y = 3.4$ nm. The interlayer spacing of graphene sheets is fixed to 0.335 nm. The distance between
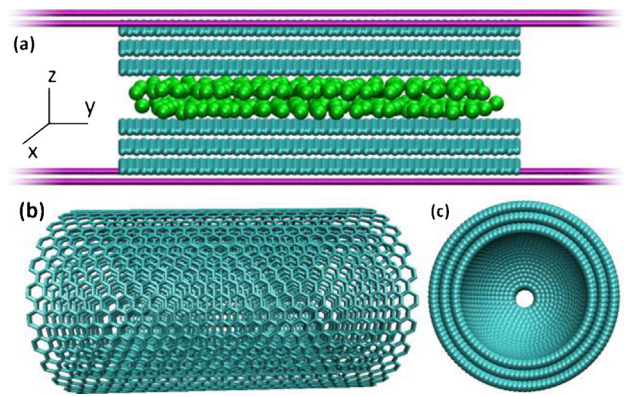

Fig. 1. Snapshots of model carbon pores: (a) carbon slit pore of finite length, (b) carbon cylindrical pore constructed from a multi-walled carbon nanotube, and (c) carbon spherical pores with a small opening. The green and blue circles represent adsorbate molecules and carbon atoms, respectively. Carbon atoms are shown at reduced scale for clarity. (For interpretation of the references to colour in this figure legend, the reader is referred to the web version of this article.).

the centre of mass of the carbon atoms in the innermost layer on opposing walls is defined as the slit pore width H. The periodic boundary conditions are only applied in the x-direction, while hard wall boundaries are applied in the y- and z-directions. The y-dimension of the simulation box is three times larger than that of the graphene sheets, so that the slit pore is of finite length, and the fluid confined in the pore is in direct contact with the bulk phase of the simulation box. For the cylindrical pore (Fig. 1b), the pore walls consist of three layers of carbon nanotubes (multiwall carbon nanotube). The interlayer spacing of the tubes is fixed to 0.335 nm. The chirality parameters are varied to construct the carbon nanotube with different diameter D (defined as the distance between the centre of mass of carbon atoms on opposite sides of the pore). The length of the tube (z-dimension) is fixed to 6.8 nm, while the z-dimension of the simulation box is three times larger than that. Hard wall boundaries are applied in the z-direction, so that the pore is of finite length and the fluid confined in the pore is in direct contact with the bulk phase. For the spherical pore (Fig. 1c), the pore walls consist of three layers of carbon spherical shells. The interlayer spacing of the shells is fixed to 0.335 nm. For each wall layer, a certain number of the carbon atoms are evenly distributed on the spherical shell, so that the areal density of the carbon atoms is the same as that in a graphene sheet. A hole with a size of two fluid diameters (∼0.7 nm) is artificially carved in the wall, so that the fluid confined in the pore is in direct contact with the bulk phase. In all three pore models, hydrostatic stability is satisfied. We introduce the models of finite length pores not only for satisfying the hydrostatic stability, but also for more accurate simulation results: we found in our previous work that an infinitely large pore with periodic boundary conditions in the x- and y-directions will result in an inaccurate adsorbate structure due to the mismatch between the dimension of the periodic boundary conditions and the structure geometry of the adsorbate [11,12]. The use of a finite pore in physical contact with the bulk phase eliminates this problem.

Grand Canonical Monte Carlo (GCMC) simulations were carried out (at constant volume, temperature, chemical potential of adsorbate) to perform adsorptions in the above model carbon porous materials. For a simple adsorbate (spherical, classical, nonpolar molecules), we use Lennard-Jones (LJ) argon as adsorbate. The argon–argon (aa) and argon–carbon (aC) interaction can be expressed as $u_{mn}(r_{ij}) = 4\varepsilon_{mn}[(\sigma_{mn}/r_{ij})^{12} - (\sigma_{mn}/r_{ij})^{6}]$, where mn can be aa or aC, $\sigma_{aa} = 0.3405$ nm, $\varepsilon_{aa}/k_B = 119.8$ K

[18], $\sigma_{CC} = 0.34$ nm, $\varepsilon_{CC}/k_B = 28$ K [19], and $\varepsilon_{mn} = \sqrt{\varepsilon_{mm}\varepsilon_{nn}}$, $\sigma_{mn} = (\sigma_{mm} + \sigma_{nn})/2$ (Lorentz-Berthelot combining rules). The potential is truncated at $5\sigma_{mn}$. We also study the adsorption and pressure of carbon tetrachloride and water confined in model carbon pores. Carbon tetrachloride is also modeled as a single site spherical LJ molecule similarly as argon, with the parameter $\varepsilon_{aa}/k_B = 322.7$ K, $\sigma_{aa} = 0.5947$ nm [20]. The water–water interaction is modeled using the extended simple-point-charge (SPC/E) pair potential [21]. This model consists of a LJ site on the O atom, with parameters $\varepsilon_{aa}/k_B = 78.2$ K, $\sigma_{aa} = 0.31656$ nm, and three point charges, one of $-0.8476\,e$ on the O and one of $+0.4238\,e$ on each H atom. The water–carbon interaction consists of a LJ interaction between the O atom and the C atoms (Lorentz-Berthelot combining rules applied), and a two-body induction interaction $U_j = -\int_0^{E_j} d\mathbf{E}_j \cdot \boldsymbol{\mu}_j = -\int_0^{E_j} d\mathbf{E}_j \cdot \alpha\mathbf{E}_j$ where $\alpha = 1.958 \times 10^{-40}$ C m^2 V^{-1} [22] is the isotropic carbon atom polarizability, j is the index of the carbon atoms, and $\mathbf{E}_j$ and $\boldsymbol{\mu}_j$ are the vector electric field and dipole acting on the j-th carbon atom due to the charges on all the water molecules. Long-range interactions are cut off at 2 nm. As reported by Perera et al., simple truncation of the SPC/E potential at a cut-off of at least 1.2 nm produces results very similar to the results where Ewald sums are used to treat long-range Coulomb effects [23].

2.2. Experimental

We have used X-ray diffraction to study two types of isotropic pitch-based activated carbon fiber (ACF) samples supplied by Ad'all Company, Japan, A10 and A20, with average pore widths of 0.85 nm and 1.40 nm, respectively. The structures of empty ACF samples and the structures of ACF loaded with water and carbon tetrachloride (ACF–H_2O and ACF–CCl_4) systems were studied at 300 K using monochromatic X-ray diffraction MoK$_\alpha$ ($\lambda = 0.071069$ nm) over a wide range of wave vectors (4.30–153.10 nm^{-1}). Further details of the sample preparation and experimental method are given in an earlier paper [24]. From the experiments we determine the interlayer spacing of the graphene sheets for the unloaded A10 and A20, and for those loaded with water and carbon tetrachloride. Kaneko and co-workers [25] have characterized these materials, using adsorption-based and other methods to determine the pore size distribution, surface area and porosity.

3. Results and discussion

The normal pressure for LJ argon adsorbed in the carbon slit pore at 87.3 K and 1 bar bulk pressure is shown in Fig. 2a for various pore widths, ranging from 0.8 to 2.8 nm. The normal pressure is, due to the hydrostatic stability, constant across the slit pore for a given width (except near the pore mouth, where it changes smoothly to the bulk phase value), but oscillates in sign as the pore width, H (or in reduced unit $H^* = H/\sigma_{aa}$), increases. The amplitude of the oscillation in the normal pressure is of the order of thousands of bars, decreasing from ∼5000 bar to ∼1000 bar as the pore width increases. This pressure enhancement arises from the geometrical confinement induced compression or tension of the adsorbate phase. The oscillation of the normal pressure arises from the oscillations in the average density of the adsorbate. For example, for a pore width of $H^* = 3.0$ (or $H = 1.0215$ nm) two complete layers of argon can be accommodated, but further increase in H only increases the interlayer spacing of argon and decreases the average density as well as the normal pressure, until the pore is wide enough ($H^* \sim 3.4$ or $H \sim 1.16$ nm) to accommodate the formation of an additional layer of argon. This addition results in a rapid increase in density and compresses the fluid in the normal direction, and so the normal pressure increases sharply. The density peaks at $H^* = 3.5$ (or $H \sim 1.2$ nm), a pore width where the additional layer is completely
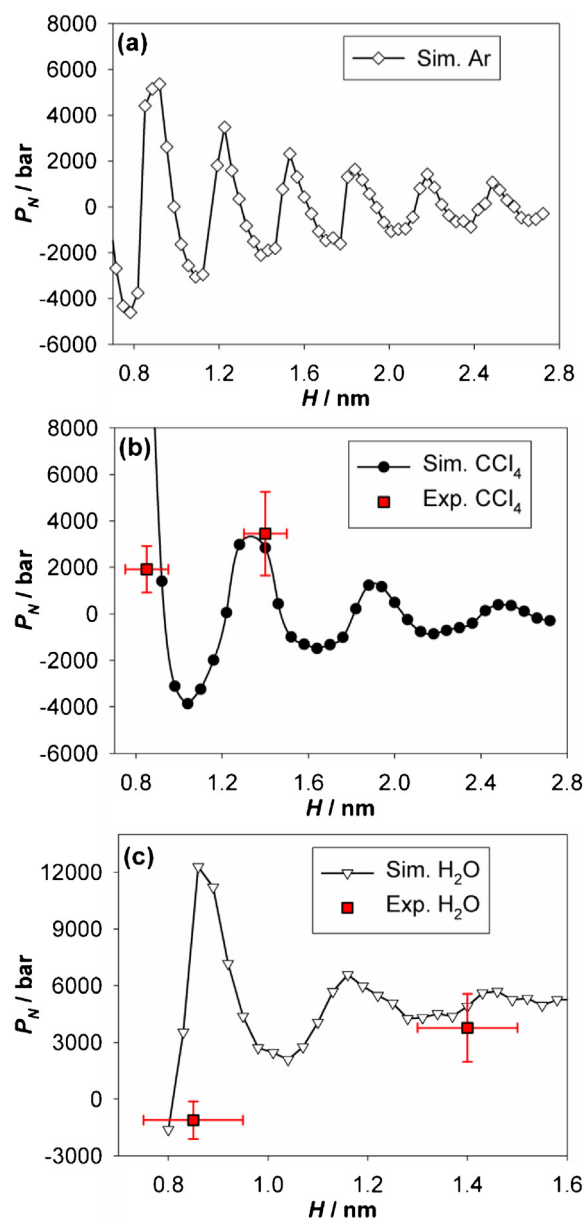

Fig. 2. The normal pressure of (a) argon (87 K), (b) carbon tetrachloride (300 K) and (c) water (300 K) as a function of the pore widths of carbon slit pores at 1 bar bulk pressure. Simulated pressure of confined water is calculated by volume perturbation method. The experimental data are included for carbon tetrachloride and water in ACF ($H = 0.85$ nm and 1.4 nm).

filled, and further increase in pore width leads to another increase in interlayer spacing of argon and decrease in density and normal pressure, until another additional layer of argon can start to form. Such oscillations in P_N and its positive and negative values result in an expansion or contraction of the pore in the normal direction. These phenomena are well known and are observed in surface force measurements [6,7] as well as in simulations and theoretical calculations [11,12,24,26].

The normal pressures of carbon tetrachloride and water adsorbed in slit carbon pore at 300 K and 1 bar bulk pressure are shown in Fig. 2(b) and (c). For carbon tetrachloride, modeled as a LJ spherical molecule, the normal pressure oscillates from positive to negative with an amplitude of thousands of bars, as was the case for argon. For water, the oscillating normal pressure is always positive except for very small pores ($H < 0.82$ nm), which is expected from the strong non-wetting behavior for water on

Table 1
The interlayer spacings (d_{002}) of graphene sheets in ACF samples with the pores empty and loaded with adsorbates.

Samples	Pore width /nm	Empty pores d_{002}/nm	Loaded d_{002}/nm	
			H_2O	CCl_4
A10	0.85	0.364	0.378	0.340
A20	1.40	0.378	0.330	0.333

carbon. Such positive oscillating pressures have been observed for water on mica surfaces in surface force apparatus experiments [27]. Our X-ray diffraction experiments measure the deformation of ACF due to adsorption of carbon tetrachloride and water, and these can be used to estimate the normal pressure on the pore walls. From the X-ray scattering we found that the average pore widths were 0.85 nm and 1.4 nm for A10 and A20, respectively; and the interlayer spacing between carbon graphene sheets were 0.364 and 0.378 nm, respectively, before adsorption. After loading with carbon tetrachloride and water at 300 K and 1 bar bulk pressure, the interlayer spacings of carbon graphene sheets were changed in A10 and A20. These changes are shown in Table 1. Using Young's equation $P_N = -\sigma_N = -E_T (\Delta d_{002}/d_{002})$, the normal pressure of the adsorbate on the wall can be roughly estimated, provided that the transverse compressive modulus, E_T, is known. Here Δd_{002} is the change in the interlayer spacing d_{002}, of graphene sheets due to adsorption. The transverse compressive modulus E_T for these pitch-based fibers has been estimated to be ∼2.9 GPa, with an uncertainty of ∼50% [24]. With this value of E_T, Young's equation predicts experimental normal pressures for carbon tetrachloride of +1912 (±956) bar and +3452 (±1726) bar, and for water −1115 (±558) bar and +3683 (±1842) bar for A10 and A20, respectively. The negative normal pressure for water in A10 indicates that the pore wall is attracted by the adsorbate, and the interlayer spacing of graphene sheets is increased. These experimental pressures are also included in Fig. 2(b) and (c) with error bars.

To study the effects of pore geometry on the normal pressure, we show in Fig. 3 the results for LJ argon in slit, cylindrical and spherical carbon pores at 87 K and 1 bar bulk pressure. The oscillation in the normal pressure with increasing pore size is observed for all three geometries. Only for the slit pore case are the oscillations regular in their behavior, with approximately constant wavelength and monotonically decreasing amplitude as pore width increases. In cylindrical and spherical pores, the oscillation of the normal pressure is more complicated. In cylindrical and spherical pores P_N shows smaller amplitude of oscillation (less than 2000 bar) than for the slit pore (∼5000 bar), and more interestingly, unless the pore is small (pore diameters smaller than 5 molecular diameters) the normal pressure is always negative. The complication in the shape of the oscillation in P_N for cylindrical and spherical pores is due to additional factors arising from the curvature of the pore walls. As the pore diameter is increased, oscillations in average density will occur as new adsorbed layers form as for the slit case, but superimposed on this is the fact that different layers can include different numbers of molecules, and this number depends on how far the layer is from the centre of the pore.

In Fig. 4 we compare the adsorbate density and pressure profiles in slit and spherical pores (at 87 K and 1 bar bulk pressure). In the slit pore (Fig. 4a), the density profile (as a function of $z^* = z/\sigma_{aa}$) shows the well-known layering effects of confinement. Seven well defined layers of argon are clearly observed as expected. The normal pressure is approximately −600 bar and is constant through the pore. The tangential pressure follows the density profile, with a peak value of 18,000 bar located at the contact layer (the layer of adsorbed argon in contact with the pore wall). For the spherical pore, we omit the results near the pore centre ($\rho^* \to 0$, or practically
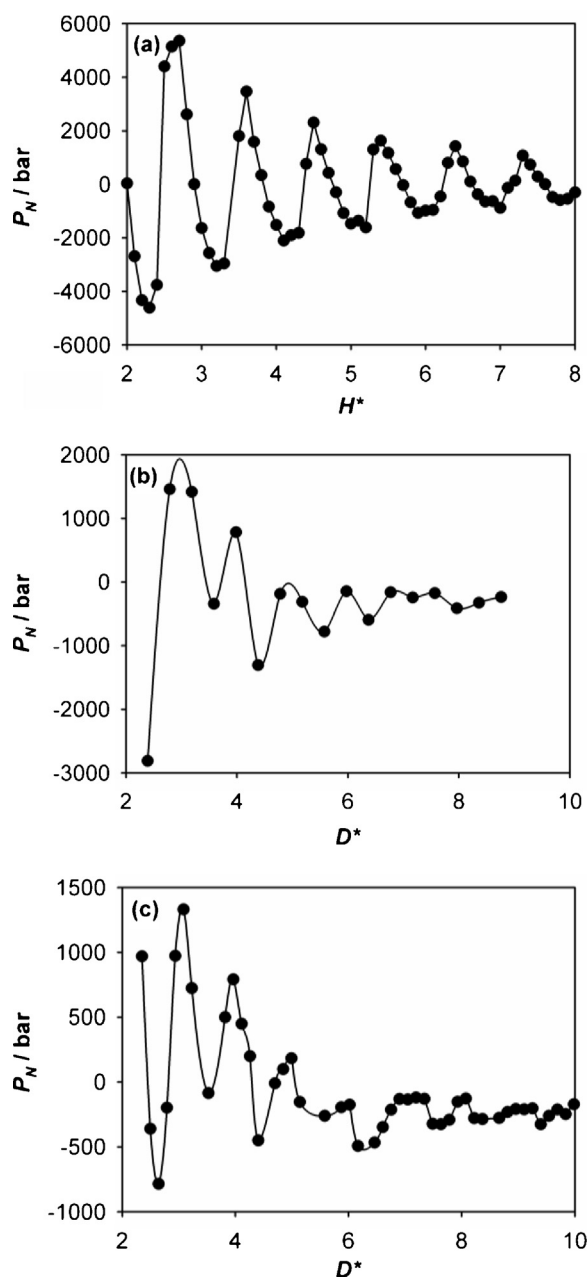

Fig. 3. The normal pressure of adsorbed LJ argon acting on the wall of (a) slit, (b) cylindrical, and (c) spherical carbon pores, at 87 K and 1 bar bulk pressure, for various pore widths.

$\rho^* = \rho/\sigma_{aa} < 0.7$), because the statistics in this small region are very poor, and for small bin widths the density (as well as the pressure) can be arbitrarily large if there is a cluster of adsorbate in the centre point of a sphere. In Fig. 4b, the density and pressure are plotted vs. the pore radius (pore diameter $D^* = D/\sigma_{aa} = 8$). The density profile shows three spherical layers, and there is an extra cluster of adsorbate molecules in the centre which are hidden. This is expected, since if a plane is cutting through the centre of the sphere, it would intersect seven adsorbate layers (2 × 3 +1 = 7). The normal pressure is of the order of ∼100 bar. In contrast to the case for slit pores, the condition of hydrostatic equilibrium does not require that P_N remain constant in the spherical pore; rather, it varies with the radial distance from the centre. The tangential pressure profile in the spherical pore roughly follows the density profile, but the two profiles are somewhat out of phase. The peak value of the tangential
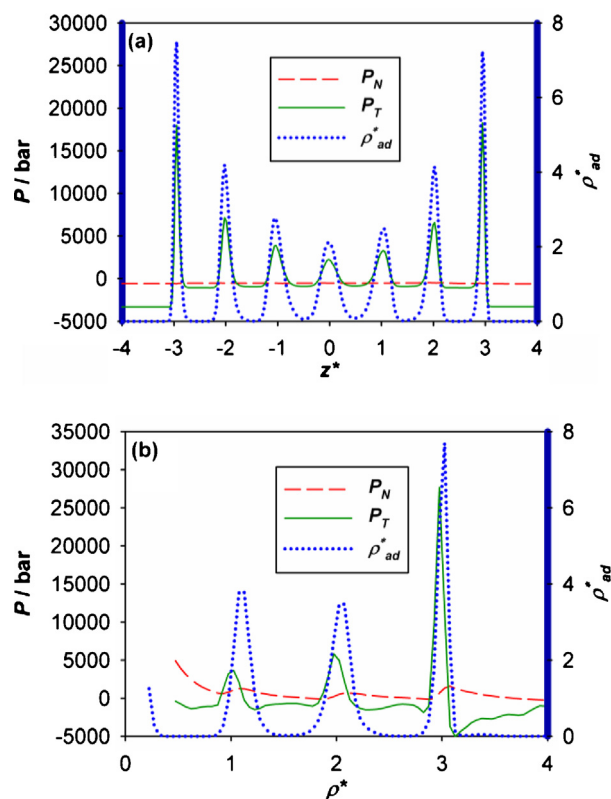
Fig. 4. The density and pressure profiles of adsorbed argon in (a) slit ($H^* = 8$) and (b) spherical ($D^* = 8$) carbon pores, at 87 K and 1 bar bulk pressure. The vertical thick solid lines represent the position of the pore wall.

Fig. 5. (a) Radial distribution function for the contact layer of confined argon at 87 K and 1 bar bulk pressure in slit (A, solid line, $H^* = 8$), cylindrical (B, dotted line, $D = 8$), and spherical (C, dashed line, $D^* = 8$) carbon pores. (b) The intermolecular pair force between two argon atoms, F, with the most probable nearest neighbor separation distances shown for the three cases illustrated in (a). The most probable separation distance for bulk argon at 87 K and 1 bar bulk pressure is also shown. (c) The adsorbate-wall energy as a function of the distance between the adsorbate molecule and the wall surface in the slit, cylindrical and spherical pores of the same pore size (H^* or $D = 8$).

pressure is ~27,700 bar, which is considerably larger than that in the slit pore. The large in-pore tangential pressure is due to the decreased separation distance between the adsorbate molecules, which is a result of the strongly attractive force field from the wall atoms [11,12]. For curved walls (cylindrical and spherical), the wall atoms provide stronger attraction to the adsorbate (more wall atoms are close to the adsorbate due to the curvature) than for the slit pore, which is shown in Fig. 5c. This compresses the adsorbate molecules more strongly and results in a smaller separation distance between neighboring molecules. The radial distribution functions for the contact layer of argon in slit, cylindrical and spherical carbon pores at 87 K and 1 bar bulk pressure are shown in Fig. 5a, and the corresponding intermolecular forces for the most probable separation distances between neighboring argon molecules for these three pores are shown in Fig. 5b. Because of the curvature and the consequent strength of the attraction from the wall, the separation distance of neighboring argon molecules in the spherical pore is smaller than that in the cylindrical pore, which in turn is smaller than in the slit pore. Thus the intermolecular force between argon molecules adsorbed in the spherical pore is the largest, followed consecutively by the cylindrical pore and slit pore.

Finally, we show the adsorption isotherms of LJ argon in slit, cylindrical and spherical carbon pores of 8 molecular diameters pore width at 87 K in Fig. 6(a). Because of the wall curvature and consequent strong attraction, argon starts to be adsorbed in the spherical pore at a bulk pressure much lower than in the cylindrical or slit pores. The condensation pressure (indicated by the second obvious jump of the isotherm) for the spherical pore is also much lower than that for the slit pore (~0.01 bar for spherical compared with ~0.25 bar for slit). The overall in-pore density of argon when the pore is fully filled is largest for the spherical pore, suggesting
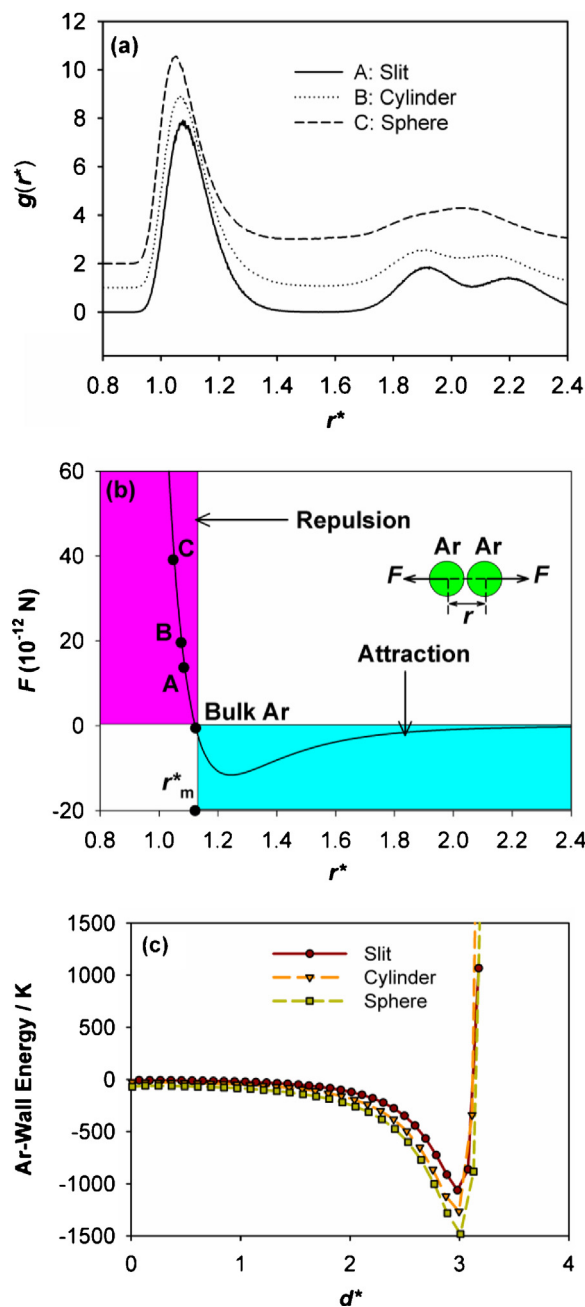
that the attraction from the wall of the spherical pore compresses the adsorbate phase more than for the cylindrical and slit pores.

The effect of bulk pressure on the in-pore tangential and normal pressures for argon adsorption in the spherical carbon pore ($D^* = 8$) at 87 K is shown in Fig. 6(b). At very low bulk pressure ($<2 \times 10^{-5}$ bar), the tangential pressure is negative with a value as large as several thousand bar, suggesting a highly attractive adsorbate-wall interaction. As the bulk pressure increases further the tangential pressure becomes positive, and increases rapidly with bulk pressure. Thus, as the bulk pressure is increased from
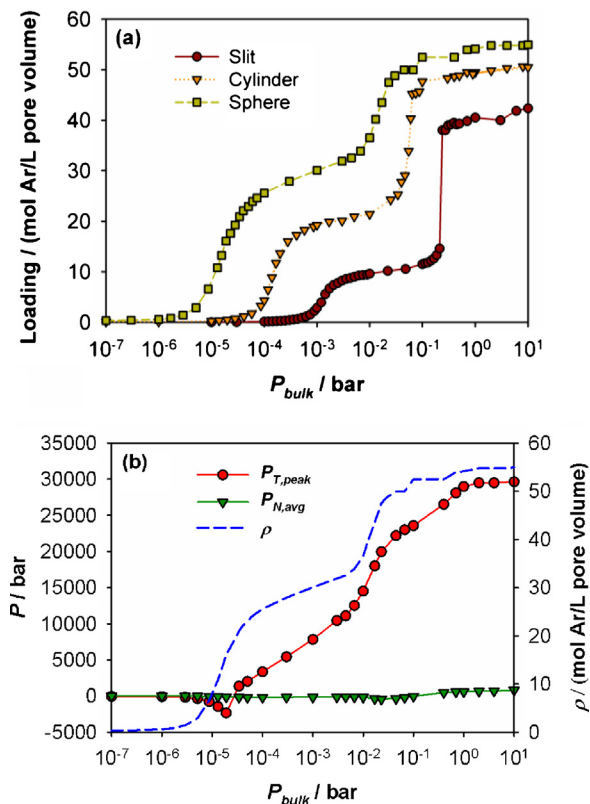
Fig. 6. (a) The adsorption isotherms of argon in slit ($H^* = 8$), cylindrical ($D^* = 8$) and spherical ($D^* = 8$) carbon pores at 87 K. (b) The peak value of tangential pressure and the normal pressure acting on the pore wall as a function of bulk pressure for argon confined in a spherical carbon pore ($D^* = 8$) at 87 K.

2×10^{-5} bar to 1 bar, the in-pore tangential pressure increases from −2000 bar to +27,700 bar. This indicates that it should be possible to explore a wide range of in-pore pressures in experiments by tuning the bulk pressure over a small range. The normal pressure of the adsorbate acting on the spherical pore wall is negative and increases in magnitude with increasing bulk pressure until the pore is almost completely filled. At large bulk pressures (e.g. >2 bar), the normal pressure becomes increasingly positive, because the high chemical potential forces more adsorbate to be accommodated in the pore, which tends to expand the pore.

4. Conclusions

We have carried out GCMC simulations for argon adsorption in slit, cylindrical and spherical carbon pores and have calculated the pressure tensor components of the confined argon phase. The calculated normal pressure oscillates as the pore width increases for all pore geometries, but the oscillations for cylindrical and spherical geometries are more complicated than for the slit pore. This increased complexity arises because as the pore radius changes there are structural changes in the adsorbate phase due to changes in the circumference of the radial adsorbed layers superimposed on changes due to inclusion or exclusion of entire layers, whereas for the slit geometry only the latter changes occur. The tangential pressure of the confined argon layer in contact with the pore wall surface is larger for the spherical pore than for the slit pore, because the separation distance between the neighbouring argon molecules in the spherical pore is smaller than in the slit pore due to the curvature of the wall. The study of the radial distribution function shows that an increase in wall curvature leads to stronger attraction from

the wall and more compression in the confined phase, and hence a larger tangential pressure. We also study the normal pressure of water and carbon tetrachloride confined in the slit carbon pore. From experimental observations of changes in the carbon interlayer distance due to adsorption, we estimate the value of the normal pressure in the pores by using the elastic modulus of ACF and Young's equation. These observed pressures are of the order of a few thousands of bars for the mean pore widths of 0.85 nm and 1.4 nm at 300 K and 1 bar bulk pressure. The simulated normal pressures agree with the experimentally estimated pressures on the wall of ACF within the (rather large) uncertainties of the latter.

Appendix

For a spherical surface, Tjatjopoulos and Mann published detailed derivations for the pressure tensor components by the IK definition [16]. A summarized derivation is presented here, and only the configurational contribution is discussed, because the kinetic part is well-defined.

Considering the identity of Dirac Delta function in spherical coordinates:

$$\delta(\mathbf{a} - \mathbf{b}) = \frac{1}{a_\rho^2 \sin a_\theta} \delta(a_\rho - b_\rho)\delta(a_\varphi - b_\varphi)\delta(a_\theta - b_\theta), \quad (A.1)$$

the general equation for the configurational pressure tensor (the second term in Eq. (3)) can be written as

$$\mathbf{P}_{conf,IK}(\mathbf{r})$$
$$= -\frac{1}{2}\left\langle \sum_{i \neq j}^{N} \frac{du(\mathbf{r}_{ij})}{d\mathbf{r}_{ij}} \frac{\mathbf{r}_{ij}}{\rho^2 \sin\theta} \int_0^1 \delta(\rho - l)\delta(\varphi - l_\varphi)\delta(\theta - l_\theta)d\lambda \right\rangle, \quad (A.2)$$

where $\mathbf{r} = \rho\mathbf{e}_\rho + \theta\mathbf{e}_\theta + \varphi\mathbf{e}_\varphi$ is the position where the pressure tensor is evaluated, and $\tilde{l} = l\mathbf{e}_\rho + l_\theta\mathbf{e}_\theta + l_\varphi\mathbf{e}_\varphi = \lambda\mathbf{r}_{ij} + \mathbf{r}_i$ ($0 \leq \lambda \leq 1$) is the integral contour, where $\mathbf{e}_\rho$, $\mathbf{e}_\theta$, and $\mathbf{e}_\phi$ are unit vectors at evaluated positions (not constants as in the Cartesian system).

As discussed previously, for a spherically symmetric system, the pressure tensor depends only on the radius coordinate, ρ. The configurational normal pressure can be obtained by averaging over the ρ-surface, where the surface area $A_\rho = 4\pi\rho^2$:

$$P_{conf,N}(\rho) = \frac{1}{4\pi} \int_0^{2\pi} d\varphi \int_0^\pi d\theta \sin\theta[\mathbf{e}_\rho(\theta, \varphi) \cdot \mathbf{P}_{conf}(\mathbf{r}) \cdot \mathbf{e}_\rho(\theta, \varphi)] \quad (A.3)$$

By substituting Eq. (A.2) into Eq. (A.3) and considering the following identity:

$$\int_0^1 f(\lambda)d\lambda = \int_{-\infty}^{+\infty} f(\lambda)\theta(\lambda)\theta(1 - \lambda)d\lambda. \quad (A.4)$$

the configurational normal pressure by IK definition, after appropriate mathematical manipulation, can be rewritten as:

$$
\begin{aligned}
P_{conf,N,IK}(\rho) \\
= -\frac{1}{8\pi\rho^2} \left\langle \sum_{-\infty}^{+\infty} \int_{-\infty}^{+\infty} (d\lambda) \left[\mathbf{e}_l . \frac{du(\mathbf{r}_{ij})}{d\mathbf{r}_{ij}} \right] \left[\mathbf{r}_{ij} . \mathbf{e}_l \right] \right. \\
\left. \times\; \delta(\rho - l)\theta(\lambda)\theta(1-\lambda) \right\rangle,
\end{aligned}
$$

$$(A.5)$$

where $\mathbf{e}_l = \mathbf{e}_\rho$ evaluated at $\tilde{\ell}$ is the unit radial vector in the direction of the vector $\tilde{\ell}$. Also note that, in Eq. (A.5), the scalar l is a function of λ.

A necessary condition that a particular pair ij will contribute to the stresses acting on the ρ-surface is that the argument of the Dirac Delta function in Eq. (A.5) is zero:

$$
f(\lambda) = \rho - l(\lambda) = \rho - \|\lambda\mathbf{r}_{ij} + \mathbf{r}_i\| = 0. \tag{A.6}
$$

The roots of Eq. (A.6) can be obtained by solving the quadratic equation:

$$
r_{ij}^2\lambda^2 + 2\lambda\mathbf{r}_{ij}.\mathbf{r}_i + \rho_i^2 - \rho^2 = 0. \tag{A.7}
$$

Mathematically, there would be 0, 1 or 2 real roots for Eq. (A.7), depending on its discriminant. Furthermore, considering the Heaviside unit step functions in Eq. (A.5), only the roots lying between 0 and 1 will contribute. Geometrically, if the straight joining line between the particles i and j crosses the ρ-surface (a spherical shell) n times ($n = 0, 1$ or 2), the intermolecular force will contribute to the pressure tensor evaluated at the ρ-surface n times. In Fig. 1 of [16], six different cases are illustrated schematically.

If the real roots of Eq. (A.7) are repeating (or sometimes regarded as a single real root), a trivial value of $(\mathbf{r}_{ij}\cdot\mathbf{e}_l)$ will result, and thus only the case of non-repeating real roots needs to be considered. We denote these two distinct real roots of Eq. (A.7) as $\alpha_{k(ij)}$, and the normal pressure by IK definition in a spherical surface can be derived as (after appropriate mathematical manipulations):

$$
\begin{aligned}
P_{conf,N,IK}(\rho) = -\frac{1}{8\pi\rho^2} \left\langle \sum_{i\neq j}\sum_{k=1}^{2} \frac{|\mathbf{r}_{ij}\cdot\mathbf{e}_l(\alpha_{k(ij)})|}{r_{ij}} \right. \\
\left. \times\; \frac{du(r_{ij})}{dr_{ij}} \theta(\alpha_{k(ij)})\theta(1-\alpha_{k(ij)}) \right\rangle,
\end{aligned} \tag{A.8}
$$

where $\boldsymbol{e}_l(\alpha_{k(ij)}) = \tilde{\ell}(\alpha_{k(ij)}) / \left\| \tilde{\ell}(\alpha_{k(ij)}) \right\|$.

The configurational tangential pressure of a spherical surface (P_T or $P_{\phi\phi}$) can be derived similarly by spatially averaging over the appropriate surfaces. The detailed derivation is also discussed in [16], and a brief outlined derivation is presented here. Consider a ϕ-surface defined by $\rho \in [\rho - \Delta, \rho + \Delta]$, $\theta \in [0, \pi]$, and $\phi = $ constant, and ρ is the radial position where the pressure tensor is evaluated, and Δ is a tiny radial increment (small compared to the molecule diameter). Then the configurational tangential pressure can be averaged as:

$$
P_{conf,T}(\rho) = \frac{1}{2\pi\rho\Delta} \int_0^\pi (d\theta) \int_{\rho-\Delta}^{\rho+\Delta} (d\rho)\rho[\mathbf{e}_\varphi(\varphi)\cdot\mathbf{P}_{conf}(\mathbf{r})\cdot\mathbf{e}_\varphi(\varphi)]. \tag{A.9}
$$

By substituting Eq. (A.2) into Eq. (A.9) and after appropriate mathematical manipulations, the configurational tangential pressure can be written as:

$$
\begin{aligned}
P_{conf,T,IK}(\rho) = -\frac{1}{4\pi\rho\Delta} \left\langle \sum_{i\neq j} \int_{-\infty}^{+\infty} d\lambda \left[\mathbf{e}_\varphi(\varphi)\cdot\frac{du(\mathbf{r}_{ij})}{d\mathbf{r}_{ij}} \right] [\mathbf{r}_{ij}\cdot\mathbf{e}_\varphi(\varphi)] \right. \\
\times\; \frac{1}{l\sin l_\theta} \times \theta(\rho + \Delta - l)\theta(l - \rho + \Delta)\theta(\lambda)\theta(1-\lambda) \\
\left. \delta(\varphi - l_\varphi) \right\rangle.
\end{aligned} \tag{A.10}
$$

The interaction of the ij pair contributes to the configurational tangential pressure if the argument of the Dirac Delta function in Eq. (A.10) is zero, i.e., the root of the following equation provides a single value of λ (which should also be between 0 and 1):

$$
f(\lambda) = \varphi - l_\varphi(\lambda) = \varphi - \arctan\frac{y_i + \lambda y_{ij}}{x_i + \lambda x_{ij}} = 0. \tag{A.11}
$$

By solving for Eq. (A.11), a single root is obtained:

$$
\lambda_{ij} = \frac{y_i - x_i\tan\varphi}{x_{ij}\tan\varphi - y_{ij}}. \tag{A.12}
$$

The final expression for the configurational tangential pressure is then given by:

$$
\begin{aligned}
P_{conf,T,IK}(\rho) = \frac{-1}{4\pi\rho\Delta} \left\langle \sum_{i\neq j} |\mathbf{r}_{ij}\cdot\mathbf{e}_\varphi| \frac{u'(\mathbf{r}_{ij})}{r_{ij}} \theta(\rho + \Delta - l(\lambda_{ij}))\theta(l(\lambda_{ij}) \right. \\
\left. -\rho + \Delta)\theta(\lambda_{ij})\theta(1-\lambda_{ij}) \right\rangle,
\end{aligned} \tag{A.13}
$$

where the unit vector $\mathbf{e}_\phi = -\mathbf{e}_x\sin\phi + \mathbf{e}_y\cos\phi$.

References

[1] K. Kaneko, N. Fukuzaki, K. Kakei, T. Suzuki, S. Ozeki, Enhancement of no dimerization by micropore fields of activated carbon-fibers, Langmuir 5 (1989) 960–965.

[2] O. Byl, P. Kondratyuk, J.T. Yates, Adsorption and dimerization of NO inside single-walled carbon nanotubes–an infrared spectroscopic study, J. Phys. Chem. B 107 (2003) 4277–4279.

[3] M. Jazdzewska, M.M. Śliwinska-Bartkowiak, A.I. Beskrovnyy, S.G. Vasilovskiy, S.W. Ting, K.Y. Chan, L.L. Huang, K.E. Gubbins, Novel ice structures in carbon nanopores: pressure enhancement effect of confinement, Phys. Chem. Chem. Phys. 13 (2011) 9008–9013.

[4] K. Urita, Y. Shiga, T. Fujimori, T. Iiyama, Y. Hattori, H. Kanoh, H. Tanaka, M. Yudasaka, S. Iijima, I. Moriguchi, F. Okino, M. Endo, K. Kaneko, Confinement in carbon nanospace-induced production of KI nanocrystals of high-pressure phase, J. Am. Chem. Society 133 (2011) 10344–10347.

[5] H.W. Hu, G.A. Carson, S. Granick, Relaxation-time of confined liquids under shear, Phys. Rev. Lett. 66 (1991) 2758–2761.

[6] J. Klein, E. Kumacheva, Confinement-induced phase-transitions in simple liquids, Science 269 (1995) 816–819.

[7] J. Klein, E. Kumacheva, Simple liquids confined to molecularly thin layers. I. Confinement-induced liquid-to-solid phase transitions, J. Chem. Phys. 108 (1998) 6996–7009.

[8] E. Kumacheva, J. Klein, Simple liquids confined to molecularly thin layers. II. Shear and frictional behavior of solidified films, J. Chem. Phys. 108 (1998) 7010–7022.

[9] Y. Fujiwara, K. Nishikawa, T. Iijima, K. Kaneko, Simulation of small-angle X-ray-scattering behavior of activated carbon–fibers adsorbing water, J. Chem. Soc., Faraday Trans. 87 (1991) 2763–2768.

[10] G. Gunther, J. Prass, O. Paris, M. Schoen, Novel insights into nanopore deformation caused by capillary condensation, Phys. Rev. Lett. 101 (2008) 086104.

[11] Y. Long, J.C. Palmer, B. Coasne, M. Śliwinska-Bartkowiak, K.E. Gubbins, Pressure enhancement in carbon nanopores: a major confinement effect, Phys. Chem. Chem. Phys. 13 (2011) 17163–17170.

[12] Y. Long, J.C. Palmer, B. Coasne, M. Śliwinska-Bartkowiak, K.E. Gubbins, Under pressure: quasi-high pressure effects in nanopores, Micropor. Mesopor. Mat. 154 (2012) 19–23.

[13] C.G. Gray, K.E. Gubbins, C.G. Joslin, in: Theory of Molecular Fluids. 2. Applications, Sec. 8.3, Oxford University Press, Oxford, 2011.

[14] J.R. Henderson, Potential-distribution theorem mechanical stability and kirk-wood integral-equation, Mol. Phys. 48 (1983) 715–717.

[15] J.P.R.B. Walton, D.J. Tildesley, J.S. Rowlinson, J.R. Henderson, The pressure tensor at the planar surface of a liquid, Mol. Phys. 48 (1983) 1357–1368.

[16] G.J. Tjatjopoulos, J.A. Mann, The pressure tensor of an inhomogeneous fluid—transformation of the Irving-Kirkwood formula, Mol. Phys. 60 (1987) 1425–1432.

[17] E. De Miguel, G. Jackson, Detailed examination of the calculation of the pressure in simulations of systems with discontinuous interactions from the mechanical and thermodynamic perspectives, Mol. Phys. 104 (2006) 3717–3734.

[18] C.R. Fuselier, J.C. Raich, N.S. Gillis, Equilibrium-configurations of commensurate adsorbed monolayers—argon on graphite, Surf. Sci. 92 (1980) 667–680.

[19] W.A. Steele, Physical interaction of gases with crystalline solids.1. Gas–solid energies and properties of isolated adsorbed atoms, Surf. Sci. 36 (1973) 317–352.

[20] H. Arstila, O.V. Vasilev, M. Kulmala, The role of the attractive potential of a droplet in unary and binary steady state nucleation, J. Chem. Phys. 107 (1997) 544–549.

[21] H.J.C. Berendsen, J.R. Grigera, T.P. Straatsma, J. Phys. Chem. 91 (1986) 6269.

[22] T.M. Miller, B. Bederson, Adv. Atomic Mol. Phys. 13 (1977) 1.

[23] L. Perera, U. Essmann, M.L. Berkowitz, Effect of the treatment of long-range forces on the dynamics of ions in aqueous-solutions, J. Chem. Phys. 102 (1995) 450–456.

[24] M. Śliwinska-Bartkowiak, H. Drozdowski, M. Kempinski, M. Jazdzewska, Y. Long, J.C. Palmer, K.E. Gubbins, Structural analysis of water and carbon tetra-chloride adsorbed in activated carbon fibres, Phys. Chem. Chem. Phys. 14 (2012) 7145–7153.

[25] J. Miyawaki, T. Kanda, K. Kaneko, Hysteresis-associated pressure-shift-induced water adsorption in carbon micropores, Langmuir 17 (2001) 664–669.

[26] P.B. Balbuena, D. Berry, K.E. Gubbins, Solvation pressures for simple fluids in micropores, J. Phys. Chem. 97 (1993) 937–943.

[27] U. Raviv, P. Laurat, J. Klein, Time dependence of forces between mica surfaces in water and its relation to the release of surface ions, J. Chem. Phys. 116 (2002) 5167–5172.